Supporting Information

Dual-Polarization Analog 2D Image Processing with Nonlocal Metasurfaces

Hoyeong Kwon[1], Andrea Cordaro,[2,3] Dimitrios Sounas,[4] Albert Polman,[3] and Andrea Alù[1,5,6,7*]

[1]Department of Electrical and Computer Engineering, The University of Texas at Austin, Austin, TX, USA

[2]Van der Waals-Zeeman Institute, Institute of Physics, University of Amsterdam, Science Park 904, 1098 XH Amsterdam, The Netherlands

[3]Center for Nanophotonics, AMOLF, Science Park 104, 1098 XG Amsterdam, The Netherlands

[4]Department of Electrical and Computer Engineering, Wayne State University, Detroit, MI, USA

[5]Photonics Initiative, Advanced Science Research Center, City University of New York, New York, NY, USA

[6]Physics Program, Graduate Center, City University of New York, New York, NY, USA

[7]Department of Electrical Engineering, City College of The City University of New York, NY, USA

*aalu@gc.cuny.edu

The purpose of this supporting information is to explain the theoretical foundations of our paper and provide further details that are not explained in the paper.

1. Nonlocality of Fano resonance

The key idea behind our design is to use the nonlocality of the Fano resonance, which realizes a certain system response as a function of spatial Fourier components. By engineering the coupling weights within the Fano resonance, the metasurface supports different spatial frequency resolutions or different types of operations. Here, we describe the Fano resonance by considering the coupling between two resonance systems and analyze how to engineer the transfer function of the metasurface by controlling the coupling coefficient of a discrete state q, and a system energy with respect to the transverse momentum $k_\parallel = k_0 \sin\theta$, as shown below. [1],[2]

$$|T(k_\parallel)| = \frac{(\varepsilon(k_\parallel)+q)^2}{\varepsilon(k_\parallel)^2+1}. \tag{S1}$$

Here, $\varepsilon(k_\parallel)$ defines how largely the frequency of the impinging wave is detuned from the resonance frequency of the system as, $\varepsilon(k_\parallel) = 2(\omega - \omega_0(k_\parallel))/\Gamma$, where Γ is the linewidth of the Fano shape and $\omega_0(k_\parallel)$ is the resonance frequency that is dispersive to the incident angle θ. [1]

In Fig. S1, we show that the Fano line shape can be controlled with the coupling coefficient q, where the asymmetric transmission profile is achieved with $q = 1$. This asymmetric shape disappears and turns to symmetric shape when q is detuned to 0 or ∞, where one of two resonant modes is dominant to another mode.
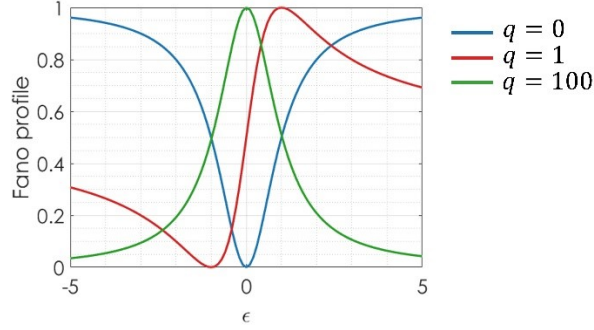
Figure. S1. The transmission of the Fano resonance when $q = 0, 1,$ and 100.
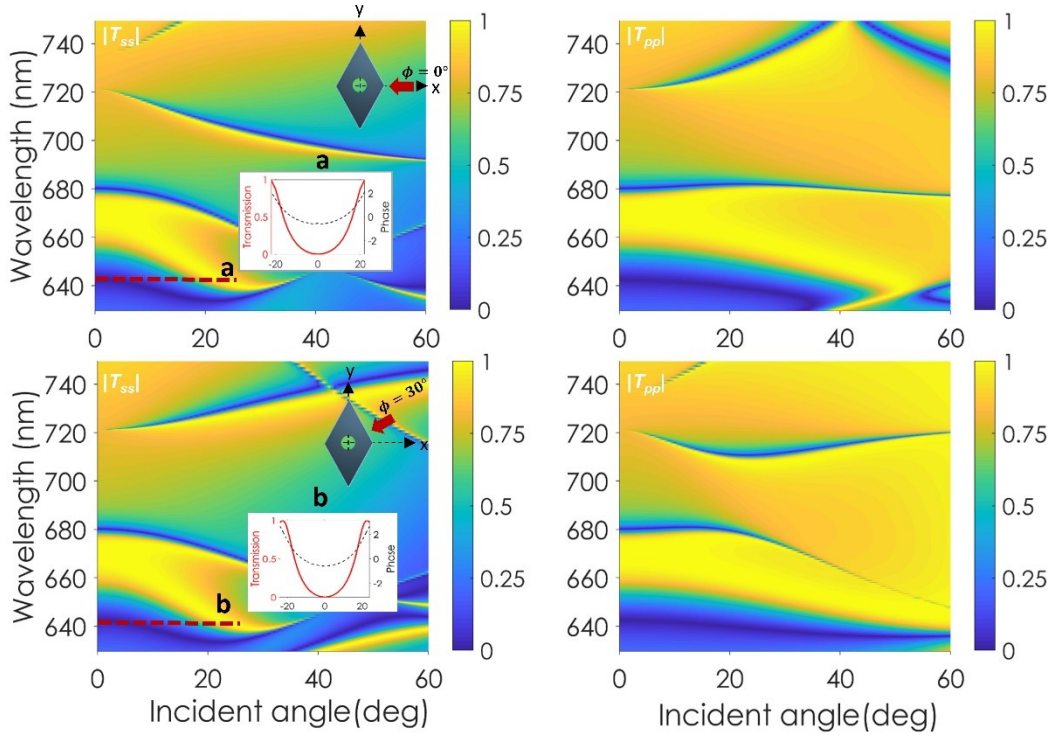
Figure. S2. Transmission amplitude of co-polarized light over a broad frequency range and angular spectrum. For both *s*- and *p*-polarizations, the metasurface achieves the 2nd-order differential operation at $\lambda = 643$nm. The top figures are the results when the light is illuminated from $\phi = 0°$, and the bottom figures are the results when the light is illuminated from $\phi = 30°$.

As mentioned in the main text, in this study, the metasurface induces a Fano resonance by coupling the leaky wave mode from the lattice and the background Fabry-Perot resonance from the thickness of the metasurface. By exciting leaky wave resonance, the frequency of Fano resonance is directly related to the resonance frequency of the discrete state as $\vec{k}_\parallel + \vec{k}_r$. This implies that the spatial dispersion of the Fano resonance can be dominantly engineered to be faster or slower in the incident angular spectrum with a proper engineering of the lattice periodicity a in the metasurface. [3]

Fig. S2 shows the numerically calculated transmission in a broad wavelength range and wide angular spectrum regarding the metasurface in Fig. 1b, where the material loss is not considered in the calculation. Supported by the lattice symmetry in the transverse direction, the metasurface supports strong nonlocality both at $\phi = 0°$ and $\phi = 30°$ modulating the transmission at the incident angular spectra, where at the resonance wavelength of normal incidence, the metasurface supports the 2nd-order differential operation, as shown in the inset figures. Spatial dispersion of this angular dependence can be engineered with the coupling coefficient q based on the theoretical analysis in Eq. (S1), where the practical analysis with the geometry of the metasurface is provided in Section 3.

2. Spatial frequency resolution – NA

When a 2D optical input image is illuminated from the far field, the field can be expressed as a collection of different transverse momentums as $\vec{E}_{in}(\vec{k}_\parallel) = \sum_{k_\parallel=0}^{k_{max}} \vec{E}_0(\vec{k}_\parallel)\exp\{-j(\vec{k}_\parallel \cdot \vec{r}_\parallel)\}$. If the input image is projected onto a metasurface that supports a specific mathematical operation with transfer function $\overline{\overline{T}}(\vec{k}_\parallel)$, each spatial component of the input image is modulated by the transmission components 'on-the-fly' through the metasurface. Fig. S3a describes the relationship between the transverse momentum of the input signal and the system function of the metasurface. Here, the transmission is a 2×2 tensor, which describes the responses of s- and p-polarized input signals. Then, the output image after the metasurface is derived as a sum of transverse momentums and represented as $\vec{E}_{out}(\vec{k}_\parallel) = \sum_{k_\parallel=0}^{k_{max}} \overline{\overline{T}}(\vec{k}_\parallel) \cdot \vec{E}_0(\vec{k}_\parallel)\exp\{-j(\vec{k}_\parallel \cdot \vec{r}_\parallel)\}$ in spatial frequency domain. The transmission is calculated orthogonally with each electric field component, as described in the main text.

The spatial frequency resolution of the operation is controlled by two important factors, the diffraction limit, and the maximum transverse momentum k_{max}. First, the diffraction limit is governed by the periodicity of the metasurface. To have the single solution after the operation, the periodicity is required to support only the lowest diffraction channel satisfying the relation $|\vec{k}_{m+n\geq1}| > |\vec{k}_0|$ under the k_{max} of our interest, where m and n are

3

the orders of diffraction. In this study, we are utilizing the triangular lattice, therefore, the diffraction orders are defined by two reciprocal lattice vectors, $\vec{b}_1 = -\frac{2\pi}{a}\left(\frac{1}{\sqrt{3}}\hat{x} + \hat{y}\right)$ and $\vec{b}_2 = -\frac{2\pi}{a}\left(\frac{1}{\sqrt{3}}\hat{x} - \hat{y}\right)$.

Fig. S3b shows the normalized transverse propagation vector, $k^{nol}_{m+n=1} = |k_{m+n=1}|/k_0$, for the mode $m + n = 1$, and describes the relationship between the diffraction limit and the maximum incident angle of the operation θ_{max}. The white dashed circle in the figure is the diffraction limit θ_{diff}, which supports a single diffraction channel in all transverse direction. For the incident angle smaller than θ_{diff}, $k_{m+n=1}$ exceeds k_0 and only the single mode $k_{m+n=0}$ exists, while the incident angle larger than θ_{diff} supports propagating $k_{m+n=1}$ under k_0. Therefore, the computational metasurface operating 2D domain has to be designed optimally within the diffraction limit θ_{diff}, always satisfying $|\vec{k}_{m+n=1}| > |\vec{k}_0|$ in all azimuthal angle of incidence.

The spatial frequency resolution, which is directly related to the optical resolution, is determined by k_{max} as described in the main text and quantized as a numerical aperture NA. The relation between NA and the maximum propagation momentum k_{max} is defined as NA $= k_{max}/k_0 = \sin\theta_{max}$, which in turn, θ_{max} determines the sharpness of the calculation, essentially the pixel size of the output. Following the discrete Fourier transform, the pixel size of the operation can be defined as π/k_{max}.[4]
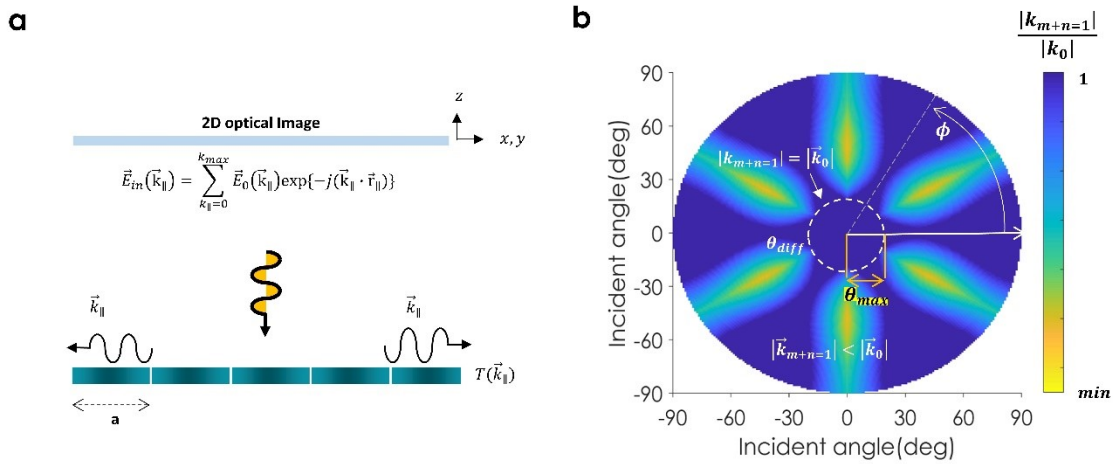

Figure. S3. (a) Analog signal processing when the 2D optical input image impinges on the computational metasurface. (b) Relationship between the diffraction limit and the maximum angle of incidence in transverse momentum space. The color scale is truncated to a unitary to clearly show the diffraction limit.

4

3. 2D operation with different polarization bases.

Next, we describe how we analytically calculate the linearly polarized 2D optical input with the metasurface, where the input image is composed of x- and y-polarizations. Assuming that the input signal is polarized to the x- and y-axes with different amplitude, the electric field can be represented as $E_x^{in}(x, y)$ and $E_y^{in}(x, y)$ as described in the main text. These field components become $\tilde{E}_x^{in}(k_x, k_y)$ and $\tilde{E}_y^{in}(k_x, k_y)$ after performing spatial Fourier transform, with the same amplitude in the space domain. For the transmission derived within the sp-polarization basis, we first decompose the field in transverse domain and convert them into xy-polarization basis following the description in Fig. S4a. Then, we can calculate the output signal in the spatial frequency domain with the transmission $\bar{\bar{T}}(k_x, k_y)$ as below.

$$\begin{pmatrix} \tilde{E}_s^{out}(k_x, k_y) \\ \tilde{E}_p^{out}(k_x, k_y) \end{pmatrix} = \begin{pmatrix} \tilde{T}_{ss}(k_x, k_y) & \tilde{T}_{sp}(k_x, k_y) \\ \tilde{T}_{ps}(k_x, k_y) & \tilde{T}_{pp}(k_x, k_y) \end{pmatrix} \overbrace{\begin{pmatrix} \sin\phi & \cos\phi \\ -\cos\phi & \sin\phi \end{pmatrix}}^{\text{Polarization converter } \bar{\bar{R}}} \begin{pmatrix} \tilde{E}_x^{in}(k_x, k_y) \\ \tilde{E}_y^{in}(k_x, k_y) \end{pmatrix}. \quad \text{(S2)}$$

Here, we define the polarization converter matrix $\bar{\bar{R}}$ between xy- and sp-polarization bases. After deriving the output in the spatial frequency domain, we multiply the inverse matrix of the polarizations converter $\bar{\bar{R}}^{-1}$ to the output to transform it back to xy-polarization basis as it is described in Fig. S4b. The final form of outputs can be derived by taking the inverse Fourier transform as $E_x^{out}(x, y)$ and $E_y^{out}(x, y)$ as displayed in the Eq.(1) in the main text. The squared value of this field amplitude is what we measure experimentally with a detector.

a

b

$xy - \text{to } sp - \text{polarization}$ $sp - \text{to } xy - \text{polarization}$
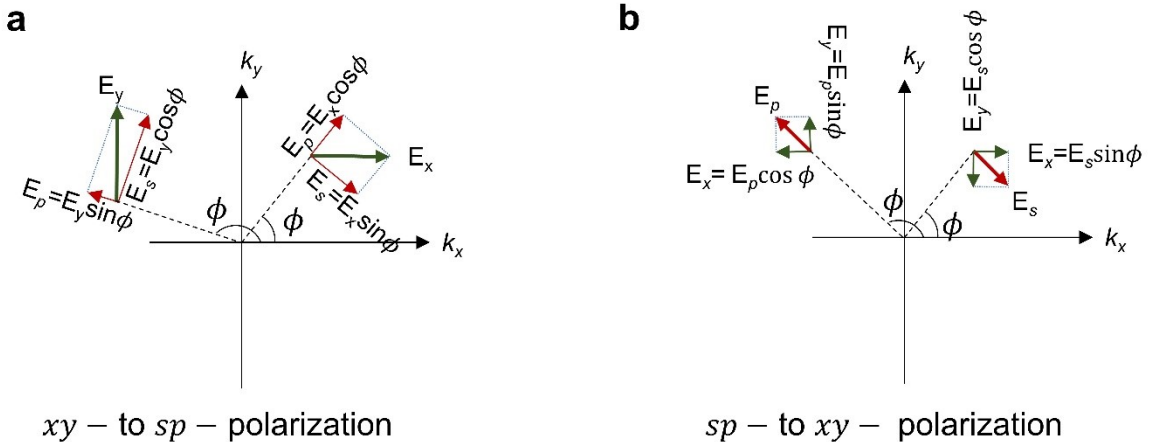
Figure. S4. (a) Electric field decomposition and synthesis into sp-polarization basis from xy-polarization basis. (b) Electric field decomposition and synthesis into xy-polarization basis from sp-polarization basis.

For unpolarized light, we assume that the field constitutes of both *x*- and *y*-components with the same intensity and random phases. Then, the average intensity of detected light is found by adding the intensities of the two orthogonal polarization components.

4. Transfer function design

Here, we provide a practical analysis to engineer the nonlocality with the metasurface and explain how to design different spatial frequency resolutions or types of operation. In a 2D triangular lattice metasurface, the radius of embedded hole at a fixed periodicity controls the coefficient q in Eq. (S1), which represents the contribution of the discrete system, and the thickness of the metasurface manages the contribution from the continuum background state within Fano resonance.
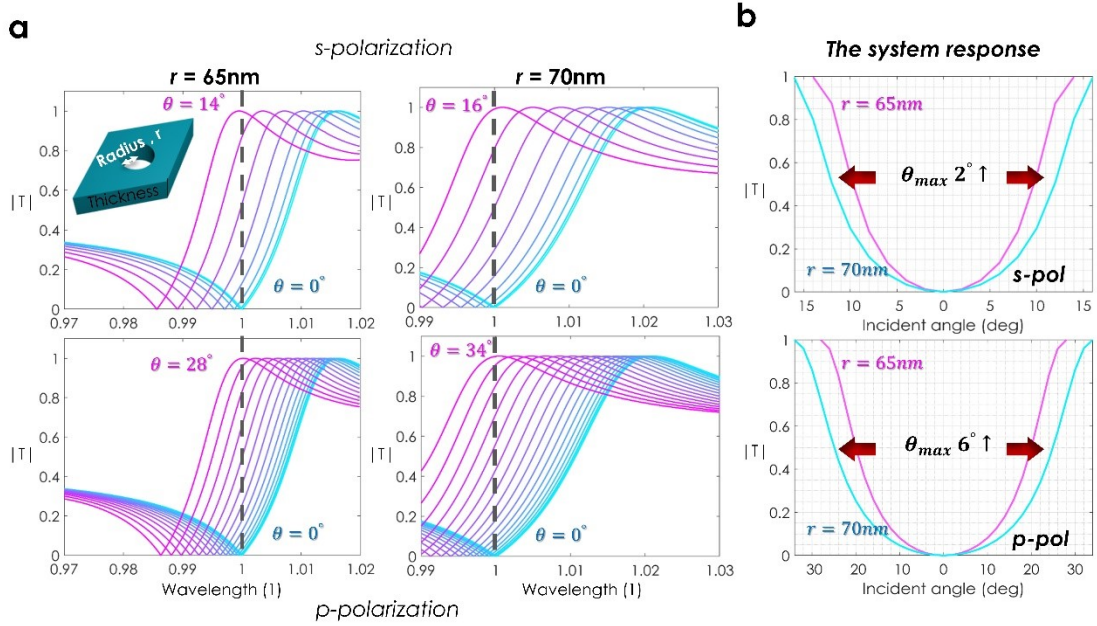
Figure. S5. The transmission as the incident angle θ is changed when the azimuthal incident angle ϕ is fixed to 0 deg. (a) The Fano responses with the different radii of cylindrical holes for both *s*- and *p*-polarizations. The wavelength is normalized with the resonance wavelength at the normal incidence. (b) The transfer function of *s*- and *p*-polarizations at a single wavelength.

First, we provide the transmission of the 2nd-order differentiator in Fig. S5, with two different radii $r = 65$nm and $r = 70$nm. Here, the loss is not considered, and the other geometries are defined to be $a = 300$nm and $t = 130$nm. Fig. S5a shows the Fano response in the wavelength spectrum as the incident angle is changed. For two different geometries, the metasurface achieves the perfect transmission at 14 deg and 16 deg toward the *s*-polarized input incidence, and at 28 deg and 34 deg toward the *p*-polarized input incidence.

6

As a result, the metasurface supports different NAs for both *s*- and *p*-polarizations, as shown in Fig. S5b, at the resonance wavelength of normal incidence. By changing the radius of the unitcell component, which contributes to the leaky wave resonance, we show that the spatial frequency resolution of the metasurface can be engineered.

Next, we address how to control the types of operation by managing the contributions from the continuum state. Here, the thickness of the metasurface is changed from $t =130$nm to $t = 180$nm with $a = 300$nm and $r = 70$nm, and the 1D transmission amplitudes are provided in Fig. S6. The Fano response with $t = 180$nm gives a different transmission curve spectrum compared to the one with $t = 130$nm, offering a symmetric dip as a function of wavelength. Here, by increasing the thickness of the metasurface, the contribution of the continuum state is largely increased compared to the discrete state and gives the symmetric transmission profile. [1]

As a result, tuning t controls the types of mathematical operations, while maintaining the same spatial frequency resolution, as shown in Fig. S6b. In the figure, the transmission profile is narrowed in the transverse momentum space with the larger contribution from the continuum state, where the line shape of the transmission is suitable for the lowest differential operation.
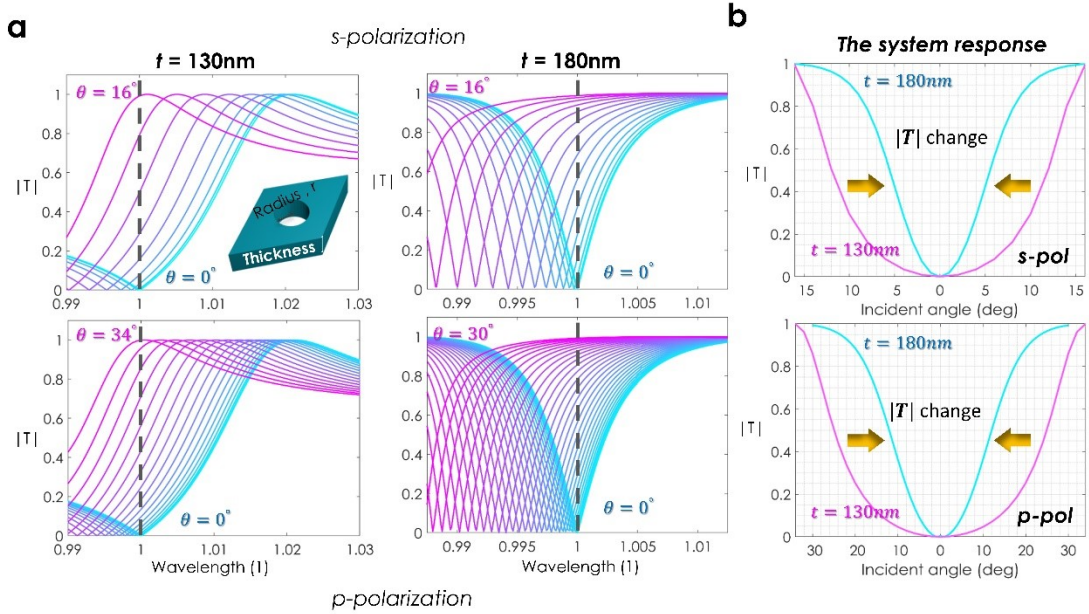

Figure. S6. The transmission as the incident angle θ is changed when the azimuthal incident angle ϕ is fixed to 0 deg. (a) The Fano responses with the different thicknesses of the metasurfaces for both *s*- and *p*-polarizations. The wavelength is normalized with the resonance wavelength at the normal incidence. (b) The system response of *s*- and *p*-polarizations at a single wavelength.

# 5. 2nd-order differential operation

5.1. Ideal system response

Fig. S7 shows the amplitude and phase of the ideal 2nd-order differentiator. Here the maximum angle of incidence is set to be 8 deg. Correspondingly, the transmission response of Fig. 1c in the main text for all angles and polarizations is shown in Fig. S8.
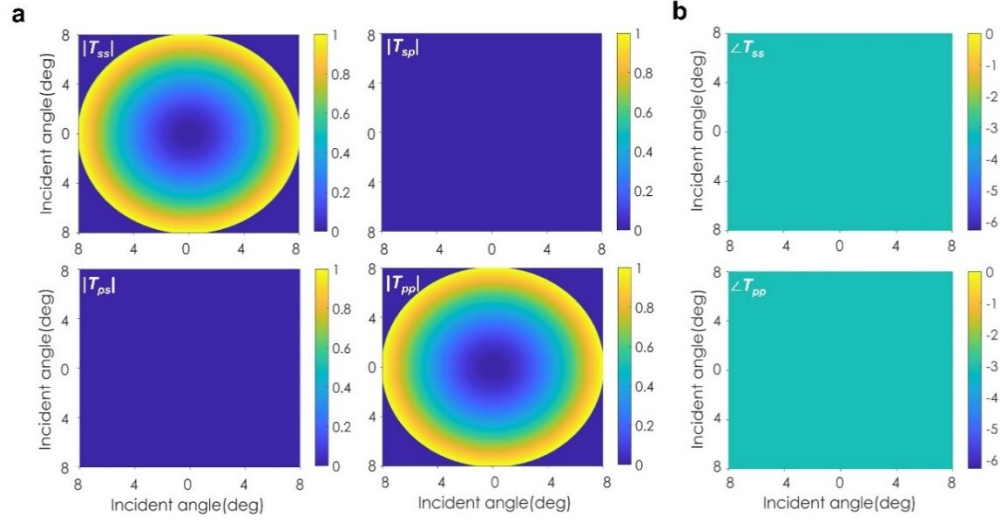
Figure. S7. (a) The transmission amplitude of the ideal 2nd-order differentiation. (b) The phase of co-polarized input incidence is flat with $-\pi$.
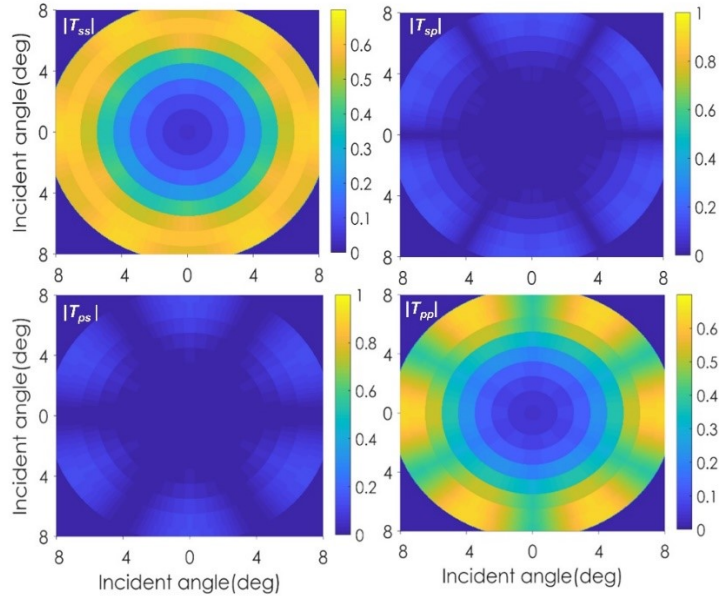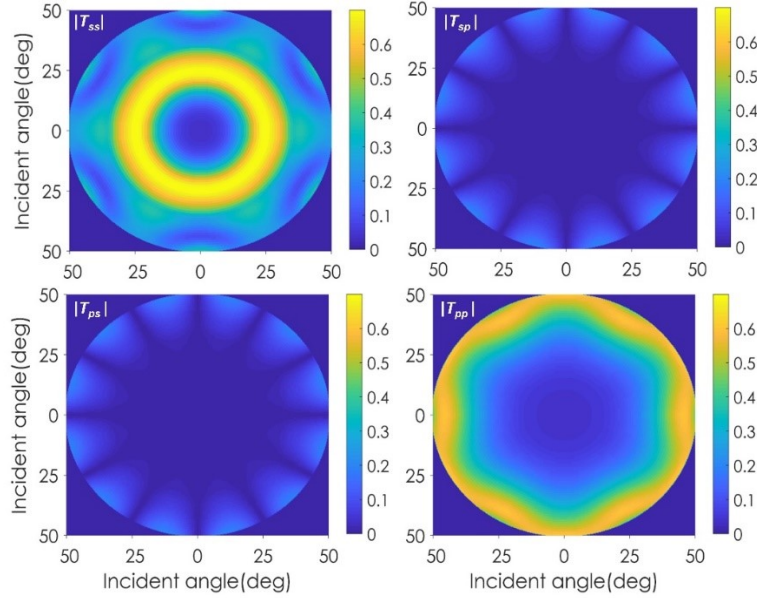

Figure. S8. Transmission amplitude of co-polarized and cross-polarized light incidence.

8

## 5.2. Different NAs between *s*- and *p*-polarizations

As we have mentioned in the main text, the metasurface can perform high-quality edge detection supported by an isotropic system response, even if it supports different NAs for two orthogonal polarizations. Here, we offer another design of the metasurface performing 2nd-order differentiation, which supports different NAs for *s*- and *p*-polarizations: NA= $\sin 25° = 0.4226$ for *s*-polarized input, and NA $= \sin 50° = 0.7660$ for *p*-polarized input as shown in Fig. S9. The metasurface is designed with $a =360$nm, $r =100$nm, $t =125$nm including material loss, and operates at $\lambda = 643$nm. The cross-polarized transmission amplitude is negligible as shown in the figure, and the phase is symmetric in transverse spatial domain supported by the structure symmetry.

Figure S9. The transmission amplitude of co-polarized and cross-polarized light incidence.

When the unpolarized 2D optical image is illuminated to the metasurface of NA $= 0.4226$, the efficiency of $|T_{pp}|$ drops to 0.1 at the maximum transverse momentum. However, supported by the isotropic system response and the analysis in Fig. S4, the metasurface can highlight edges in all transverse directions, which in turn, supports high quality edge detections in all azimuthal angles of propagation.

Fig. S10 shows the output images when the unpolarized input image in Fig. S10a is projected to the ideal system and to the metasurface under an NA $= 0.4226$. In the results, we can see that the output after the metasurface in Fig. S10c highlights the edges clearly in all transverse directions of propagations, analogous to the output after the ideal system in Fig. S10b.
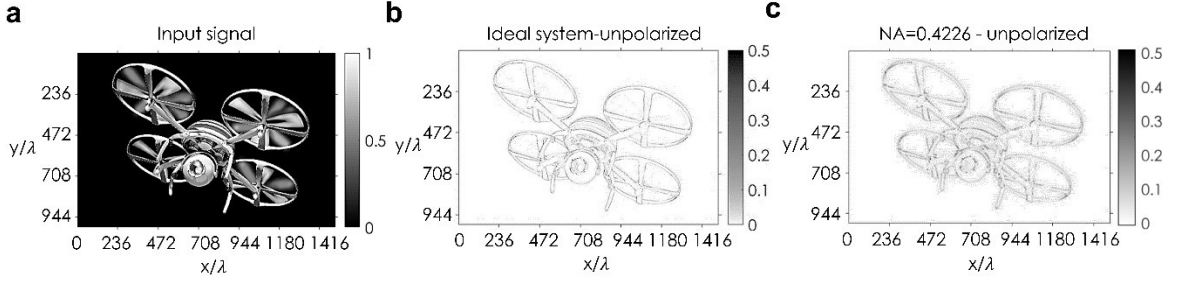
Figure. S10. (a) The complex 2D input image. (b) The output after the ideal system with NA = 0.4662 when the unpolarized input image in (a) is illuminated. (c) The output after the metasurface with NA=0.4226 when the unpolarized input image in (a) is illuminated.

## 6. 1ˢᵗ-order differential operation

6.1. Ideal system response

The ideal system response of the 1ˢᵗ-order differentiator is provided in Fig. S11. Here the amplitude is defined as $\sin\theta_{inc}$, and the phase jumps at normal incidence with π for co-polarized plane wave incidence. Here, the coefficient $A_1(\phi)$ is applied to the ideal system response with 120 deg rotational symmetry, considering the system response of the metasurface in Fig. 3b.
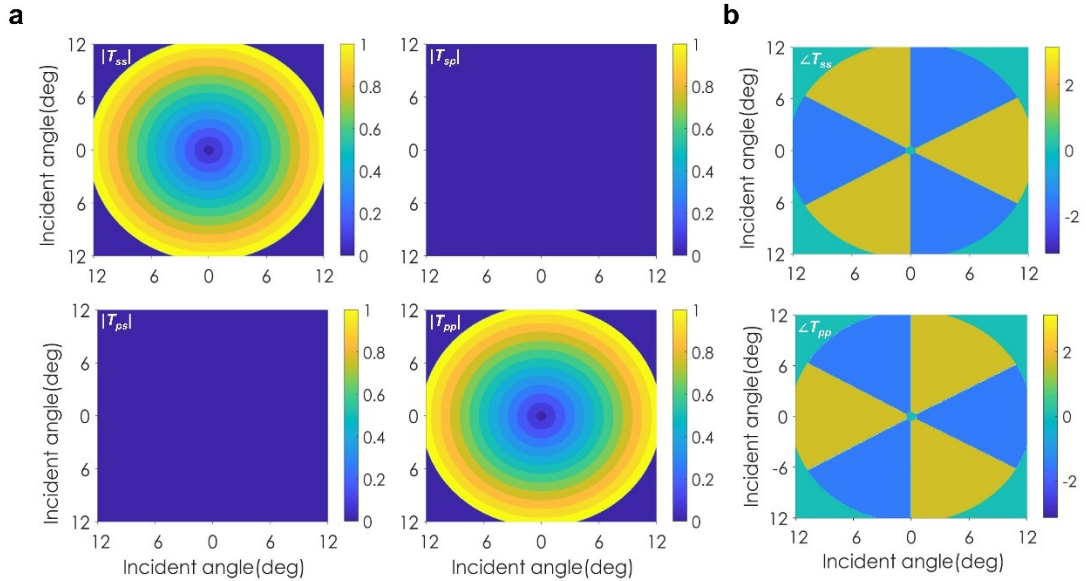
Figure. S11. The ideal system response of the 1ˢᵗ-order differential operation. (a) The transmission amplitudes for both co- and cross-polarizations. (b) The transmission phase of the co-polarized light incidence.

10

6.2. Engineering the odd phase response

As explained in the main text, a π-phase jump in the odd order differentiator can be engineered by applying the substrate to the asymmetric lattice in Fig. 3a. Here, we elucidate how to engineer the phase jump with different thickness of the substrate in Fig. S12. In the figure, phase profiles near normal incidence are plotted when the thickness of the substrate is swept from 51nm to 55nm with 1nm step, where near π-phase jumps are observed for both s- and p-polarizations. For the different thicknesses, the resonance wavelengths are slowly shifting from $\lambda = 628$nm to $\lambda = 629$nm.
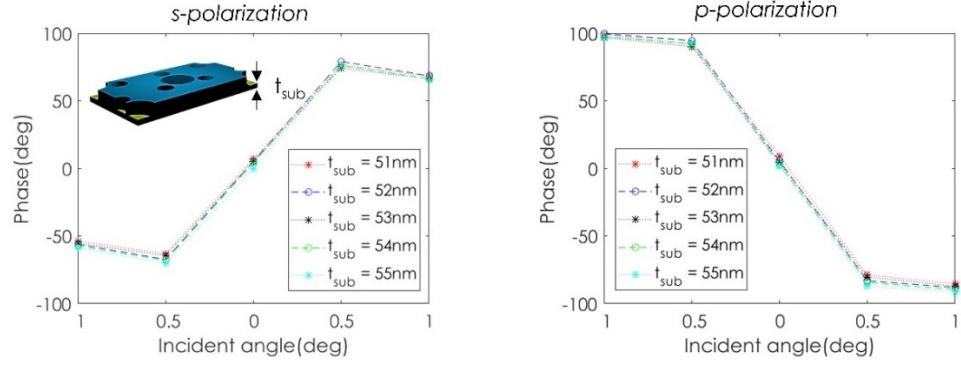
Figure. S12. The phase profile near the normal incidence with the different thicknesses of the substrate. For both s- and p-polarizations, the metasurface achieves near π-phase jump at resonance wavelength.

## 6.3. Entire transmission response in Figure 3b
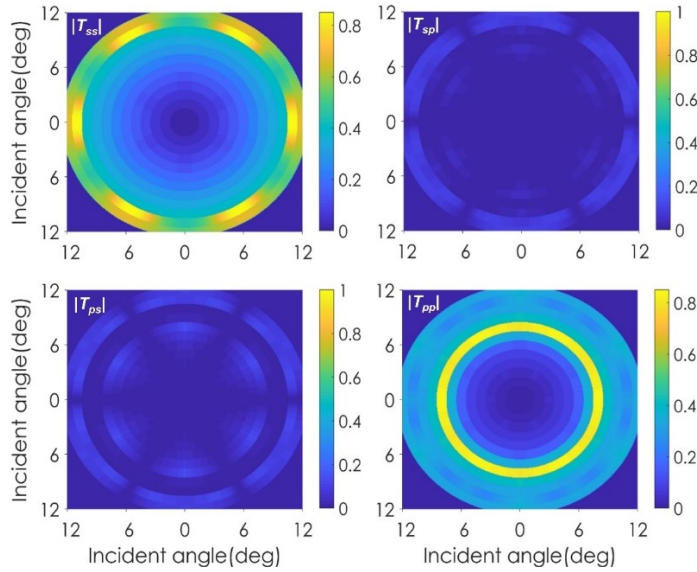
Figure. S13. The transmission amplitude of co-polarized and cross-polarized light incidence of the metasurface in Fig. 3b.

7. Comparison of 2D edge detection between 1st- and 2nd-order differential operation

In the main text, we showed that the 1st-order differentiator offers a single spike per a single edge, while the 2nd-order differentiator gives double spikes per a single edge. The results were provided with 1D input signal of a single polarization. Therefore, here, we show that this property is also preserved in the case of 2D optical operation of all transverse spatial frequency domain, by comparing the outputs of Fig. 2 and Fig. 5 in the main text.

First, we compare the outputs after the ideal system response in Fig. S14. Here, the output image is expanded to show the details of Fig. 2b and Fig. 5b with $1200 \leq x/\lambda \leq 1680, 1080 \leq y/\lambda \leq 1560$. For the input image in Fig. S14a, the output after the 1st-order differentiator gives a single solid line following the object boundary. If we look at the 1D cross-cut at $x/\lambda = 1560$ as in the bottom of Fig. S14a, we can see that the ideal 1st-order differentiator gives a single spike at the image edge as shown in the bottom of Fig. S14b.

However, the 2D output image in Fig. S14c shows double solid lines following the object boundary as a result of the 2nd-order differentiation, where the cross-cut at $x/\lambda = 1560$ gives double spikes per edge as shown in the bottom figure.
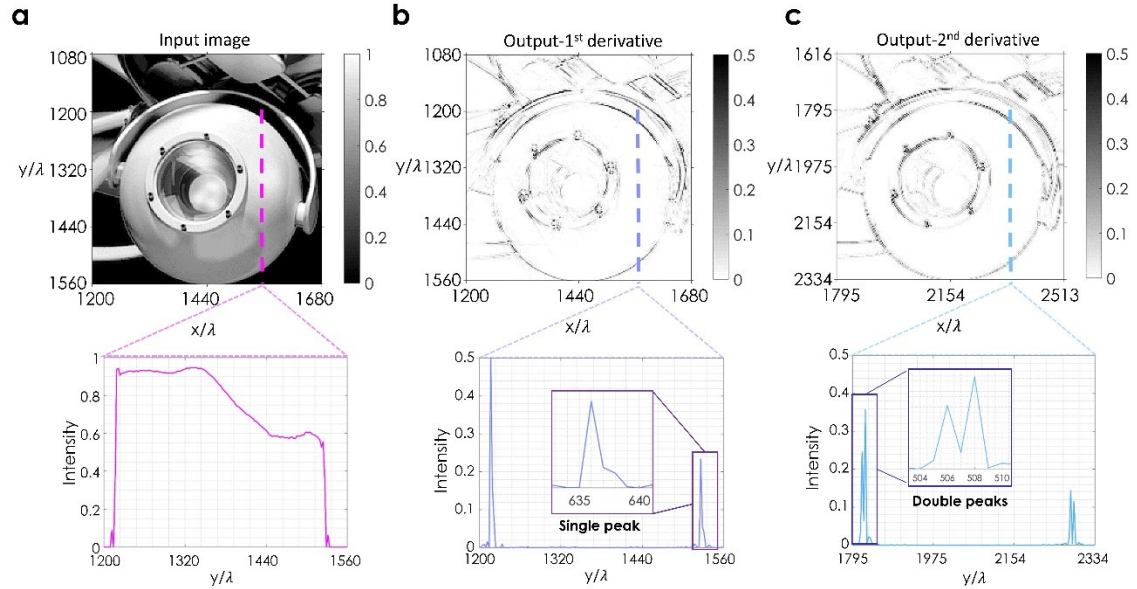
Figure. S14. The expanded 2D input and outputs after the ideal system response. The bottom 1D figure shows the 1D cross-cut intensity profile at $x/\lambda = 1560$. (a) The 2D input image (upper). The 1D input intensity gives the rectangular-like input shape (bottom). (b) The 2D and 1D outputs after the ideal 1st-order differentiator. (c) The 2D and 1D outputs after the ideal 2nd-order differentiator.

Next, we compare the output after the metasurface in Fig. S15. In the results, we can see that the output after the 1st-order differentiator also gives a single solid line following the object boundary in Fig. S15b as the ideal differentiator. The noise around the edges is small, and is induced by the phase mismatch with the ideal system. The cross-cut at the same x coordinate proves that the metasurface gives a single spike per edge as shown in the bottom figure of Fig. S15b. The output after the 2nd-order differentiator is also shown in Fig. S15c, where the metasurface output has double spikes at a single slope change, as we can expect from the ideal system response.

To conclude, the metasurface performing 1st-order differentiation appears to be more suitable for edge detection application in terms of precision and accuracy, offering single peak at the field intensity variation.
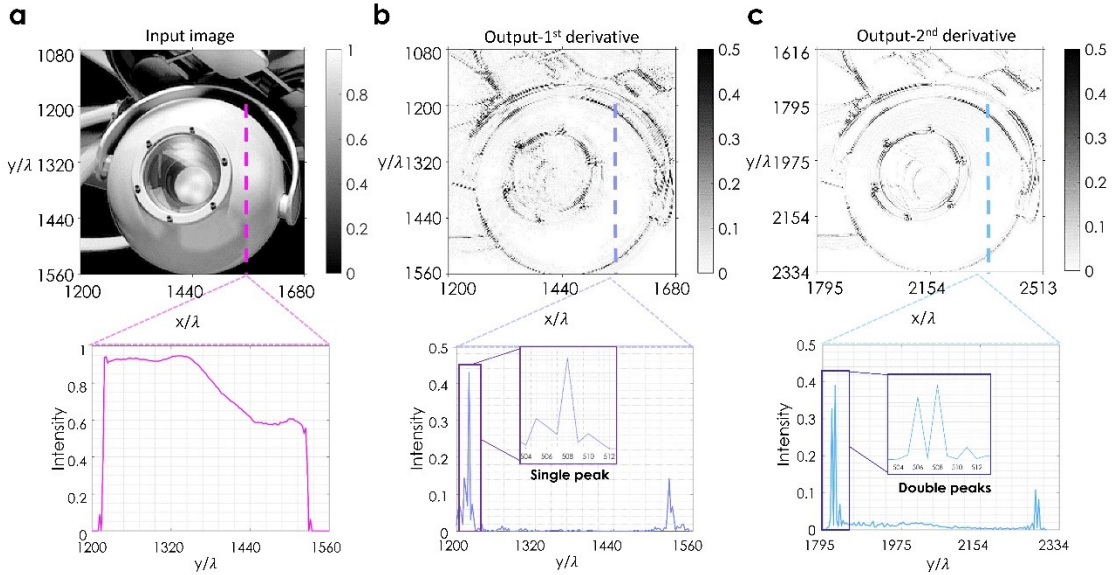

Figure. S15. The expanded 2D input and outputs after the proposed metasurface. The bottom 1D figure shows the intensity profile at $x/\lambda = 1560$. (a) The 2D input image. The 1D input intensity gives the rectangular-like input shape. (b) The 2D and 1D outputs after the metasurface in Fig. 5d. (c) The 2D and 1D outputs after the metasurface in Fig. 2d.

8. Passive integration

The metasurface can perform an even-order passive integration by properly engineering the nonlocal response and the operation wavelength. By choosing the operating frequency, where the metasurface supports zero transmission at θ_{max}, the metasurface can perform the opposite operation of an integral-like low pass filter. Here, the metasurface is optimized to $a = 300nm$, $r = 70nm$ and $t = 180nm$, and the system response is provided in Fig. S16, where NA $= \sin 13° = 0.2250$ for the s-polarized input incidence, and NA $= \sin 30° =$

0.5000 for the *p*-polarized input incidence. The operation wavelength is $\lambda = 640$nm. The phase response in Fig. S16b shows transverse symmetry in all azimuthal angles of propagations supported by the lattice symmetry.
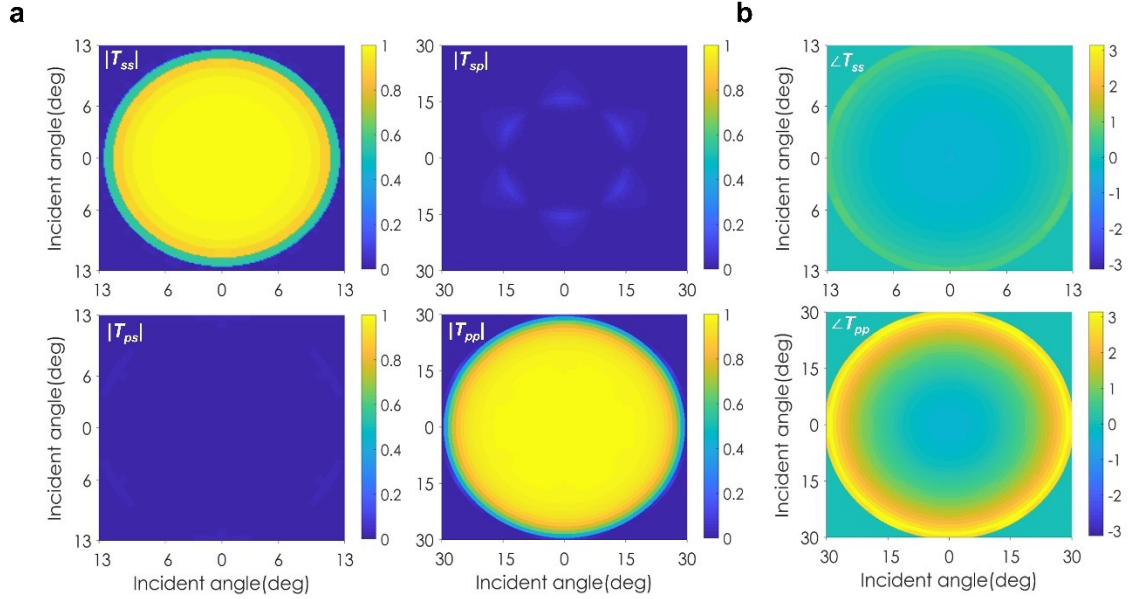
Figure. S16. The metasurface system response of the passive integral operation (a) The transmission amplitudes for both co- and cross-polarizations. (b) The transmission phase of the co-polarized light incidence.
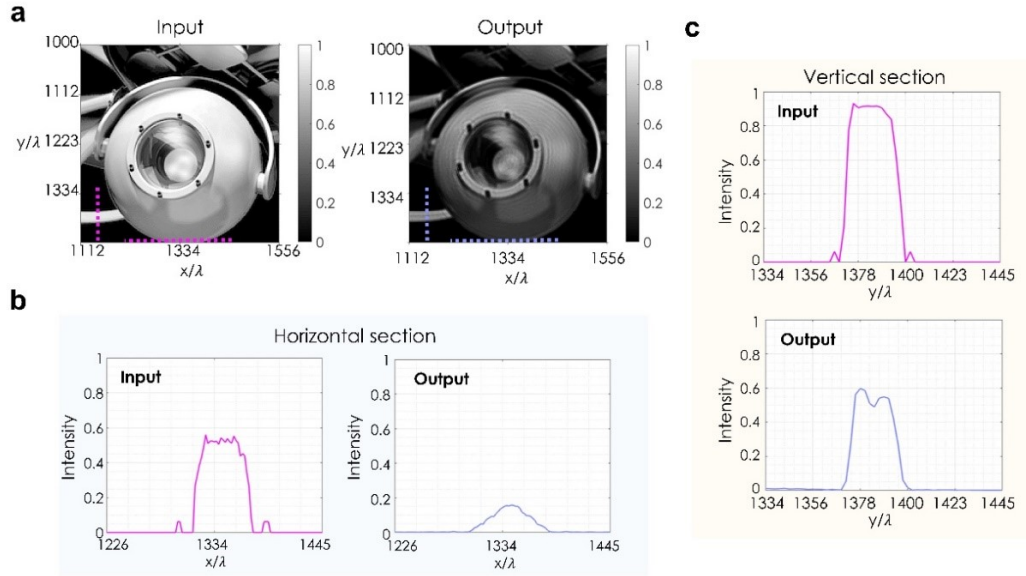
Figure S17. (a) The expanded 2D input and output after the metasurface. (b) 1D cross-cut of 2D input (horizontal dashed line in the left panel of (a)) and of 2D output (horizontal dashed line in the right panel of (a)) after the metasurface system response in Fig. S16. (c) 1D cross-cut of 2D input (vertical dashed line in the left panel of (a)) and 1D cross-cut of 2D output (vertical dashed line in the right panel of (a)) after the metasurface system response in Fig. S16.

The 2D metasurface output is provided in Fig. S17 for the same input image in Fig. S14 and S15, and line cross-cuts at $y/\lambda = 1440$ and $x/\lambda = 1156$ are provided in Fig. S17b and S17c. The results show that the sharp edges of the input image are smoothen after the metasurface, effectively filtering out the high frequency components. Here the output is calculated with NA = 0.2550. This type of metasurface can be utilized to support noise cancelling in optical image processing applications.

References

[1]   A. Cordaro, H. Kwon, D. Sounas, F. Koenderink, A. Polman, and A. Alù, High-index dielectric metasurfaces performing mathematical operations. *Nano Lett*. **2019**, 19, 1530-6984.

[2]   A. E. Miroshinichenko, Fano resonances in nonascale structure. *Rev. Mod. Phys*. **2010**, 82, 2257.

[3]   L. Novotony, B. Hecht, Principle of Nano-Optics, *Cambridge University Press*, Cambridge, 2006, 338-343.

[4]   E. Chu, Discrete and Continuous Fourier Transforms: Analysis, Applications and Fast Algorithms. *CRC Press*, Boca Raton, FL, 2008.